Icarus 420 (2024) 116197

Contents lists available at ScienceDirect

Icarus

journal homepage: www.elsevier.com/locate/icarus

Hierarchical-agglomerative clustering analysis of geomorphic features applied to tectonic investigation of terrestrial planets: An example from Claritas Fossae, Mars

Evandro Balbi [a,*], Paola Cianfarra [a], Laura Crispini [a], Silvano Tosi [b], Gabriele Ferretti [a]

[a] Università degli Studi di Genova, Dipartimento di Scienze della Terra dell'Ambiente e della Vita (DISTAV), Corso Europa 26, 16132 Genova, Italy
[b] Università degli Studi di Genova, Dipartimento di Fisica (DIFI), 16146 Genova, Italy

ARTICLE INFO

Keywords:
Cluster analysis
Claritas Fossae
Mars
Lineaments
Tectonics
Terrestrial planets

ABSTRACT

A hierarchical-agglomerative clustering workflow is proposed to investigate complex, tectonically controlled regions on planetary surfaces. This algorithm comprises two primary steps: (i) calculating the dissimilarity between each object and (ii) grouping objects using a hierarchical clustering method. The efficiency of the workflow hinges on two critical parameters that require careful selection: the attributes for grouping objects and the number of clusters for interpretation. We applied this approach to tectonic lineaments in the Claritas Fossae (CF) region on Mars, a complex area significantly shaped by tectonic activity. Our analysis considered three attributes of these lineaments: (i) azimuthal direction, (ii) length, and (iii) centroid position. The optimal number of clusters was determined using the Silhouette index (S), which assesses the robustness of the clustering results. Our objectives were twofold: (i) to replicate the distribution of lineament sets obtained from classical geostatistical analysis of their azimuthal orientation and (ii) to refine the subdivision by varying combinations of the three attributes. Our results provide crucial insights into the geo-tectonic evolution of CF, supporting the hypothesis of a tectonic evolution characterised by a polyphase history. In addition, we demonstrate how the method is capable of effectively identified areas with varying intensities of brittle deformation.

1. Introduction

Surfaces of bodies characterised by a rigid outer shell, such as terrestrial planets and icy or rocky natural satellites, are characterised by various linear and curvilinear features associated with tectonic activity. These features, referred to as tectonic lineaments, include faults, fractures, folds, grabens, semigraben-like depressions and escarpments. The identification and categorisation of tectonic lineaments, along with the analysis of their characteristics (e.g. orientation, length, spacing, sinuosity), have been highly informative on Earth (Ouillon et al., 1996; Mazzarini and D'Orazio, 2003; Mazzarini, 2007; Mazzarini and Isola, 2010; Cianfarra and Salvini, 2014; Franceschini et al., 2020; Mazzarini and Isola, 2021; Mazzarini and Isola, 2022; Ceccato et al., 2022; de Arruda Passos et al., 2022; Cianfarra et al., 2024) and on other planetary surfaces (Wise et al., 1979; Rossi et al., 2018, 2020; Anguita et al., 2001; Plescia, 2003; Pozzobon et al., 2015; Anderson et al., 2019; Lucchetti et al., 2021; Perrin et al., 2022; Man et al., 2023; Karagoz et al., 2024). These studies have helped to unravel the role of tectonics in shaping the present-day setting. To objectively categorise objects with similar characteristics, classification and clustering methods are commonly applied in Earth Science (Ansari et al., 2009; Paasche and Eberle, 2009; Yang et al., 2019; Aghaee et al., 2021; Faraj and Ortiz, 2021). Classification methods group objects into predefined target classes, whereas clustering methods sort objects into several groups. In the clustering analysis, each group comprises the most similar objects, thus it is homogeneous and distinct from others (Kaufman and Rousseeuw, 1990; Arabie et al., 1996; Mirkin, 2013; Schwenker and Trentin, 2014). Clustering algorithms are conventionally categorised into four main methods based on the adopted cluster model: partitioning, hierarchical, arbitrary origin and mutual similarity (Sneath and Sokal, 1973; Gordon, 1999). Hierarchical methods, which are widely used in tectonic investigations (Mazzarini, 2004; Davey et al., 2013; Šilhavý et al., 2016; Takahashi et al., 2019; Prabhakaran et al., 2021; Kaas et al., 2023), operate by initially grouping the most similar objects into clusters and then connecting them with the next most similar objects. This approach deals with all possible clusters in a single run, with the progression of

* Corresponding author.
E-mail address: evandro.balbi@edu.unige.it (E. Balbi).

https://doi.org/10.1016/j.icarus.2024.116197
Received 14 February 2024; Received in revised form 29 May 2024; Accepted 20 June 2024
Available online 25 June 2024

similarity levels at which objects are merged displayed as a dendrogram. There are two types of hierarchical techniques: agglomeration and division. Agglomerative methods begin with each object as a separate cluster (i.e. n objects = n clusters) and progressively merge clusters until a single cluster containing all objects is formed. Conversely, divisive methods start with all objects merged into a single cluster, subsequently the initial cluster is split until n clusters remain.

In this study, we aim at developing an analytical and statistical clustering workflow capable of providing objective insights into the geotectonic evolution of complex, tectonically controlled regions. Specifically, we present a clustering procedure based on an agglomerative hierarchical method that calculates the dissimilarity among tectonic lineaments based on a series of attributes selected for their geological significance (azimuthal direction, length and centroid position). We decided to use the agglomerative method because most recent and updated software packages (as the R package "*fastcluster*") have restricted their attention to the agglomerative hierarchical techniques which are less computationally intensive than the divisive ones. As study case, we selected the Claritas Fossae (CF) on Mars, a tectonically controlled region where the temporal and spatial relations among the different identified tectonic mechanisms and kinematics (i.e. normal dip-slip and strike slip) are still debated (Hauber and Kronberg, 2005; Montgomery et al., 2009; Balbi et al., 2024). The presented workflow proved to be effective in reducing bias related to the subjective interpretation of geostatistical data and helped to clarify the role of tectonics in the CF region.

2. Geological setting

Mars hosted intense volcanic and tectonic activity at regional and global scale throughout long period of times mainly in the first 2–2.5 billion years of the planet (i.e. Noachian, from 4.1 to 3.7 Gy, and Hesperian, 3.7 to 3.0 Gy, periods). Then, endogenous processes progressively reduced in the Amazonian period (3.0 Gy to present) (Carr and Head III, 2010). Despite the large scale of some of these events, their intensity and lifetime have not been sufficient to obliterate records of previous processes, contrary to Earth. In addition, the negligible impact of exogenous processes led the regional scale landscapes to remain unaltered from their formation to present (Golombek and Bridges, 2000; Golombek et al., 2006; Golombek and Phillips, 2010). In this way, several evidence of endogenous processes remained preserved on the surface at different scales of observation and can be analysed to reconstruct the geologic evolution of Mars. Among the numerous regional and global scale physiographic features led by endogenous processes there is the Claritas Fossae (CF). This represents the westernmost margin of the Thaumasia Region (Fig. 1A), a volcano-tectonic province located southeast of Tharsis which is bounded to the north by the Valles Marineris and Noctis Labyrinthus and to the south-southeast by the Thaumasia Highlands (Dohm and Tanaka, 1999). The CF comprises a N-S oriented and elongated deformation corridor extending over 1000 km in total length and 150 km in width. In there, a complex network of fractures, faults, scarps and ridges persist over Noachian and Hesperian terrains (Fig. 1B,C - Tanaka et al., 2014; Vaz et al., 2014; Bouley et al., 2018). Various studies associate the formation of the CF with intense tectonic activity affecting the area from the Noachian to the Amazonian periods (Dohm and Tanaka, 1999; Dohm et al., 2001; Anderson et al., 2001; Hauber and Kronberg, 2005; Smith et al., 2009; Montgomery et al., 2009; Tanaka et al., 2014). Besides evidence of both extensional and strike-slip tectonics has been identified (Hauber and Kronberg, 2005; Montgomery et al., 2009; Balbi et al., 2022, 2024), the mechanisms leading to the formation of this striking physiographic feature remains a subject of debate. The regional topography of the CF between 15°S–38°S and 95°W–115°W resembles terrestrial half-grabens. This area, termed Thaumasia Graben by Hauber and Kronberg (2005), is characterised in the east by a sharp and abrupt scarp and in the west by a gently dipping, rounded slope, informally named the Eastern Scarp

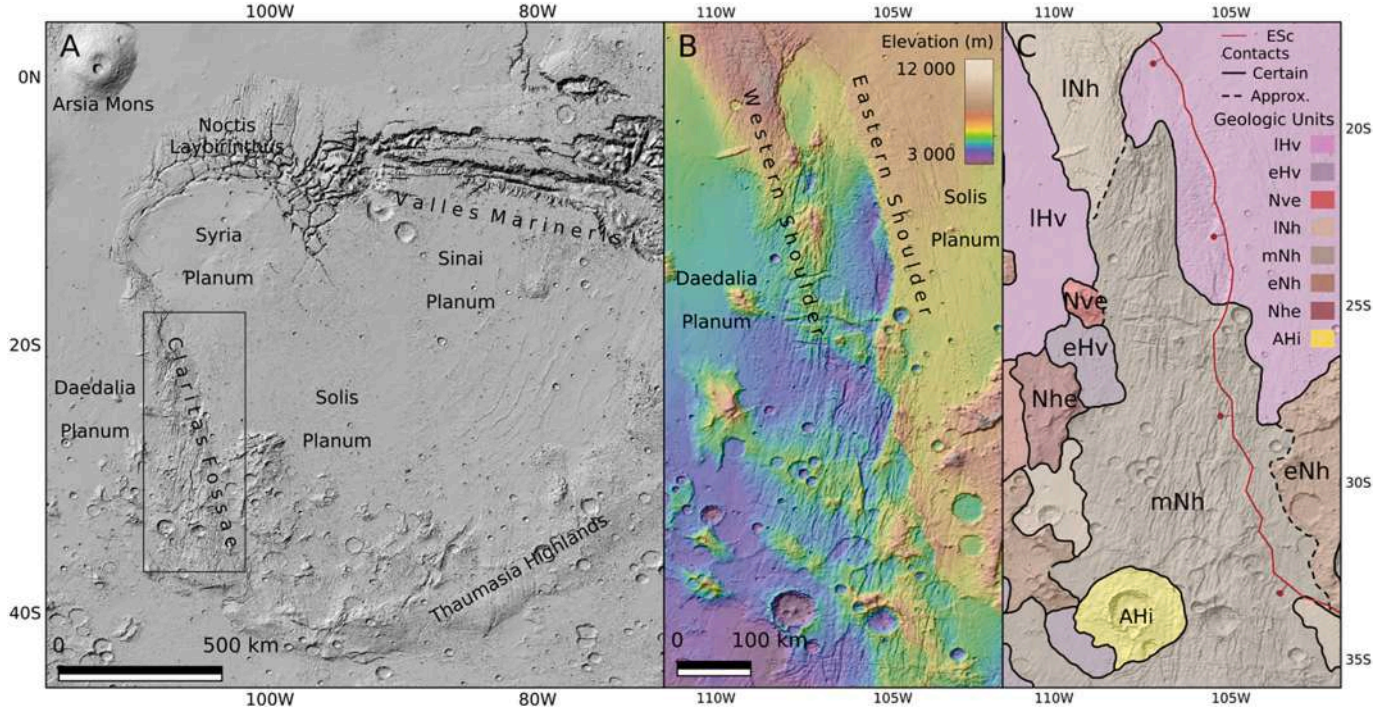

Fig. 1. A) Hillshade of the Thauamsia Region derived from Mars MGS MOLA–MEX HRSC Blended DEM Global v2. Black box indicates the study area; B) topographic map of the CF; C) Geologic Map of the CF area (modified from Tanaka et al., 2014). Legend: trace of the Eastern Scarp (ESc), red markers indicate the dip of the scarp, Volcanic Units–lHv: Late Hesperian volcanic unit; eHv: Early Hesperian volcanic unit; Nve: Noachian volcanic edifice unit; Highlands Units–lNh: Late Noachian highlands unit; mNh: Middle Noachian highlands unit; eNh: Early Noachian highlands unit; Nhe: Noachian highlands edifice unit; Widespread Units–Ahi: Amazonian and Hesperian impact unit. (For interpretation of the references to colour in this figure legend, the reader is referred to the web version of this article.)

(ESc) and the Western Shoulder (WSh), respectively (Balbi et al., 2024). The ESc, the most prominent feature at the CF, extends over 900 km between 17°S–107°W and 33°S–103°W in both Late Hesperian and Middle Noachian units. It separates the Thaumasia Plateau (or Eastern Shoulder, Esh, in Fig. 1B) from the eastern limit of the WSh, presenting an abrupt elevation change that reaches 300 m to the north, 2150 m at 24°S–105°W and then decreases southward to a nearly negligible topographic contrast. The morphological characteristics of the ESc, such as its large size and morphological offset, led researchers to propose the presence of a crustal-scale, normal fault system in an extensional tectonic setting (Plescia and Saunders, 1982; Tanaka et al., 1991; Tanaka and Davis, 1988; Hauber and Kronberg, 2005). Conversely, the presence of en-echelon arrangements, Riedel shear structures, pull-apart and restraining bend geometries (Montgomery et al., 2009; Balbi et al., 2024), along with morphological similarities to the San Andreas Fault (Yin, 2012; Dohm et al., 2015, 2018), indicate that horizontal, strike-slip tectonics also played a role. The co-existence of strike-slip and normal dip-slip tectonics evidence may imply that both mechanisms operated within a single long-term transtensional event or in two distinct stages of deformation (Balbi et al., 2024). In this respect, the CF represents a crustal-scale tectonic feature that has been active throughout Martian geological history, potentially serving as a preferential pathway for magma/fluid migration from the planet's interior to its surface and atmosphere (Pieterek et al., 2024; Balbi et al., 2024).

3. Materials and methods

3.1. Description of the dataset analysed through cluster analysis

To evaluate the reliability in geo-tectonic investigations of the proposed clustering workflow, an existing (and validated) structural dataset comprising several hundred objects was used. This dataset includes the 251 regional-scale tectonic lineaments identified in our previous work (Balbi et al., 2024) through systematic, visual inspection of enhanced subsets of two types of satellite image mosaics: Mars MGS MOLA–MEX HRSC Blended DEM Global v2 (spatial resolution 200 m/px; Fergason et al., 2018) and THEMIS Day/NightIR Controlled Mosaic (spatial resolution 100 m/px; Christensen et al., 2004; Edwards et al., 2011). These image datasets represented the best compromise between the regional scale approach and the resolution of the images and allowed the identification of the most prominent and regionally developed lineaments representative of the regional deformation. The subsets used for the regional-scale structural mapping were extracted from the original mosaics and enhanced to improve lineament recognition following the procedure described in detail in Lucianetti et al. (2017) and in Balbi and Marini (2024). The adopted procedure envisages the creation of eight synthetic lighting conditions (at intervals of 45° azimuth) from *MOLA-HRSC DEM* to mitigate bias from a single light direction (Wise et al., 1985; Balbi and Marini, 2024). High-pass Laplacian filters and look-up-table stretching were applied to the derived shadow images and the *THEMIS Day/NightIR Controlled Mosaic*, enhancing tonal contrasts (Drury, 2004). To ensure the regional-scale approach, mapping was conducted at a fixed scale of 1:5,000,000, identifying patterns of aligned pixels associated with tonal contrasts indicative of elongated topographic features >20 km in length. To ensure dataset robustness, only alignments visible in at least eight different images (i.e. six shadow images and one enhanced THEMIS image) were mapped and digitised. Digitisation involved tracing polylines and drawing vertices within a dedicated vector layer in geographic information system environment (QGIS 3.18_Zurich). The identified lineaments, indicative of regional/crustal deformation, are localised between ~20°S and ~35°S latitudes and ~102°W and ~112°W longitudes and comprise single or linked scarps characterised by significant elevation changes. They correspond to elongated topographic features, such as reliefs and graben/half-graben or to juxtapositions of regions with varying image textures (e.g. surface roughness differences). The geostatistical analysis of the azimuth of the tectonic lineaments conducted in Balbi et al. (2024) by frequency and cumulative length, revealed a subdivision into four azimuthal sets. This pattern, consistent with a Riedel shear model (Fossen, 2016), aligns with a model of strain partitioning and shear fracture orientation in a right-lateral strike-slip deformation corridor (Storti et al., 2006; Balbi et al., 2024). To test the reliability of the here proposed clustering workflow, we aimed at reproducing this subdivision of set considering for the analysis the length and the position of the lineaments together with their azimuth. Therefore, azimuthal direction, length and position were measured for each lineament, representing the attributes used for clustering. Specifically, the *azimuthal direction* is the angle (0°–180°) between the north and the fictitious linear feature connecting the extremes of the mapped lineament. *Length* is the curvilinear length of the mapped lineament, and *position* is the Euclidean distance between the centroid (defined by latitude and longitude) of the mapped lineament and the planetocentric coordinate system's origin (latitude 0°, longitude 0°) as defined in Duxbury et al. (2002).

3.2. Cluster analysis

Cluster analysis is a powerful tool for systematically identifying groups within data (Kaufman and Rousseeuw, 1990). Among the various clustering algorithms, such as partitioning methods, hierarchical clustering, arbitrary origin methods and mutual similarity procedures, hierarchical methods are increasingly utilised in multivariate data analysis. Hierarchical methods are prevalent in numerous fields, including artificial intelligence, ecology, economics, geosciences, marketing, medical research and political science. They effectively reproduce the hierarchical structure of data, classify multivariate populations and identify groups or clusters (Mojena, 1977). This study employs an agglomerative hierarchical clustering model, wherein objects (i.e. mapped tectonic lineaments) are iteratively merged into clusters based on a dissimilarity measure between observation sets. The arrangement of clusters, produced iteratively by the chosen method, is visually represented in a dendrogram (Fig. 2). To apply the clustering method, it is necessary to compute the degree of dissimilarity between the objects. This is referred to as the "distance" between objects. Initially, distance calculation involves computing all pairwise dissimilarities between objects, resulting in a dissimilarity matrix. Various distance measures can be employed, such as Euclidean, Maximum, Manhattan, Canberra, Binary, Gower or Minkowski distance (Kaufman and Rousseeuw, 1990). For instance, Euclidean distances are calculated as the root sum-of-squares of differences, Manhattan distances as the sum of absolute differences and Gower's distance is achieved using the general dissimilarity coefficient of Gower (1971). Subsequently, an agglomerative algorithm merges clusters iteratively based on their dissimilarity. This process starts with n single clusters (representing the n input objects), computes the dissimilarities among all cluster pairs and continuously merges the closest clusters until a single comprehensive cluster emerges, encompassing all original input objects. Common methods for computing distances or dissimilarities among clusters include the single linkage (the shortest distance between any two points in each cluster), the complete linkage (the maximum distance between any two points in each cluster), the average linkage (the average distance between points in two clusters) and the centroid linkage (the distance between cluster centroids in Euclidean space) (Müllner, 2013). Clearly the choice of the most suitable "distance" cannot be entirely objective, and it depends on the "characteristics" of the data to be clustered. Several tests have to be performed in order to select the distance function. In our work, after several tests we have chosen the Gower's distance because it allows the assignment of a specific weight to the attribute considered for the clustering and it leads to subdivisions of the tectonic lineaments from which significant geological implications can be derived (see 5.2 paragraph).

In this study, the clustering procedure utilises the '*daisy*' function from the R package '*cluster*' (Struyf et al., 1997) and the '*hclust*' function

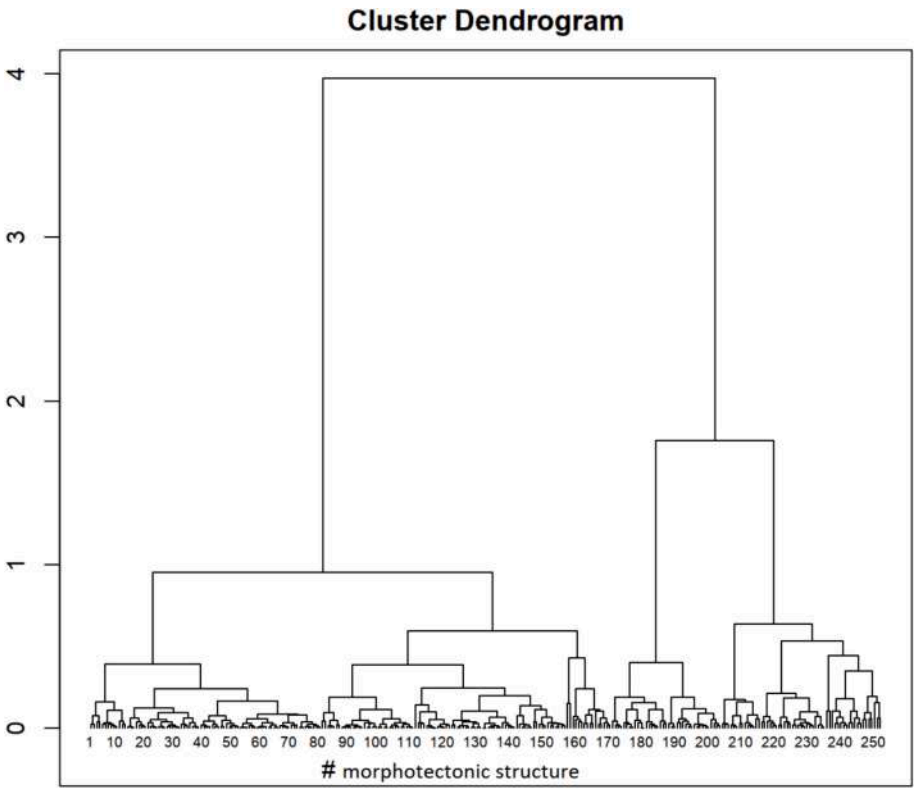

Fig. 2. Dendrogram showing the clustering of the analysed objects (e.g. tectonic lineaments in the case of our study). On X-axis the number of objects is shown, on Y-axis the height indicates the distance (i.e. degree of dissimilarity) at which two single objects or two clusters are merged in a new cluster.

from the R package *'fastcluster'* (Müllner, 2013). The '*daisy*' function computes the dissimilarity matrix by employing *Gower's distance* and assigning a specific weight to each attribute of lineaments in the dataset. Hierarchical clustering is executed using the '*hclust*' function, which employs the '*Ward.D2*' agglomeration method (Murtagh and Legendre, 2014), based on Ward Jr's (1963) clustering criterion.

A stopping rule is necessary to select the 'best' number of clusters based on the clustering criterion distribution associated with each hierarchical level. This work, following Rousseeuw (1987) and Kaufman and Rousseeuw (1990), guides the choice of the 'best' number of clusters through the computation of silhouette width *(s)*. For each object i in cluster A, *s(i)* is defined as follows:

$$s(i) = \frac{b(i) - a(i)}{max\{a(i), b(i)\}}$$

where

$a(i)$ = average dissimilarity of i to all other objects of A

and

$$b(i) = \min_{C \neq A} d(i, C)$$

where for any cluster C distinct from A, *d(i,C)* denotes the average dissimilarity between object i and its neighbouring objects in C.

The average silhouette width of a cluster is derived from the mean of the silhouette values, *s(i)*, for all objects i within that cluster. An *s(i)* (~ 1) suggests that the objects are well-clustered, whereas *s(i)* (~ 0) indicates that objects are positioned between two clusters. A negative *s(i)* implies that the objects likely be placed in the wrong cluster. The average silhouette width for the entire dataset, denoted as $\bar{s}(k)$, is calculated by averaging the *s(i)* values for all objects, $i = 1, 2, \ldots, n$, where n represents the total number of objects in the dataset. Mathematically, the "best" number of cluster may be defined by the value of k for which $\bar{s}(k)$ is as high as possible. In particular, $\bar{s}$ between 0.71 and 1 indicates a strong (robust) clustering structure, between 0.51 and 0.70 a reasonable clustering structure, between 0.26 and 0.50 a weak clustering structure, and ≤ 0.25 no substantial clustering structure (Kaufman and Rousseeuw, 1990).

In summary, the general outline of the clustering workflow proposed in this study is as follows:

a) Input data preparation: Clustering is applied to the 251 tectonic lineaments identified in the CF by Balbi et al. (2024), through structural mapping. The input data are displayed as a matrix with dimensions n x p, where n is the number of observations (i.e. 251), and p is the number of attributes (i.e. 3).
b) Scaling observations: Each attribute of the observations is corrected by subtracting the mean and dividing by the standard deviation of the entire vector.
c) Dissimilarity matrix calculation: The computation of all pairwise dissimilarities (distances) between observations in the dataset is performed using the Daisy function, selecting the metric 'Gower'. The weight for each attribute is specified by a vector of length p (the number of attributes used in the clustering).
d) Hierarchical clustering: Clustering is implemented using the 'hclust' function with the agglomeration method 'Ward.D2'. In this step, different values of k (the number of clusters) are considered as a stopping rule.
e) Validation of consistency within clusters of data: The technique 'silhouette', proposed by Rousseeuw (1987), is used to examine the clustering configuration. For each value of k, the average silhouette width, $\bar{s}(k)$is computed and the 'best' number of clusters is chosen.

4. Results

Among various tests conducted on 251 tectonic lineaments using azimuth, length and position as attributes, four were selected as

representative for evaluating the performance of the proposed clustering workflow. Three tests consider different uses of attributes in the clustering procedure, each assigning a weight of 1 to the considered attributes: 1) *azimuth* only; 2) *azimuth and length* and 3) *azimuth, length and position*. The fourth test evaluates *azimuth, length and position* by assigning double weight to azimuth compared to the other attributes.

Here, we present only the results obtained by considering, for each test, a range of clusters, *k*, from 3 to 6 (*k* being the stopping rule in the hierarchical clustering step) which are the most statistically robust and informative from a tectonic and geological point of view. Clusters formed with k > 6 are overly fragmented and demonstrate significantly low $\bar{s}(k)$ values (<0.25). Consequently, 16 outputs from the clustering procedure are discussed herein. In the text, clusters are denoted as follows: *Cluster2-Azimuth + Length-k4*. The first suffix refers to the name of the cluster (Cluster2 in this example), second to the attribute(s) used (azimuth and length) and third to the *k* value selected for that test (4).

Fig. 3A-D shows the clustering results obtained using azimuth as the sole attribute and varying *k* values (i.e. k = 3, 4, 5, 6). Clustering based solely on azimuth yield groups with average silhouette widths consistently exceeding 0.5, indicating statistically strong and, therefore, interpretable cluster structures. Fig. 3A illustrates the cluster subdivision with *k* set to 3; the three identified clusters in Azimuth-k3 comprise 54, 158 and 39 lineaments, each characterised by an average azimuth of 166°, 21° and 92°, respectively (Table 1). In Fig. 3B, where k is set to 4,

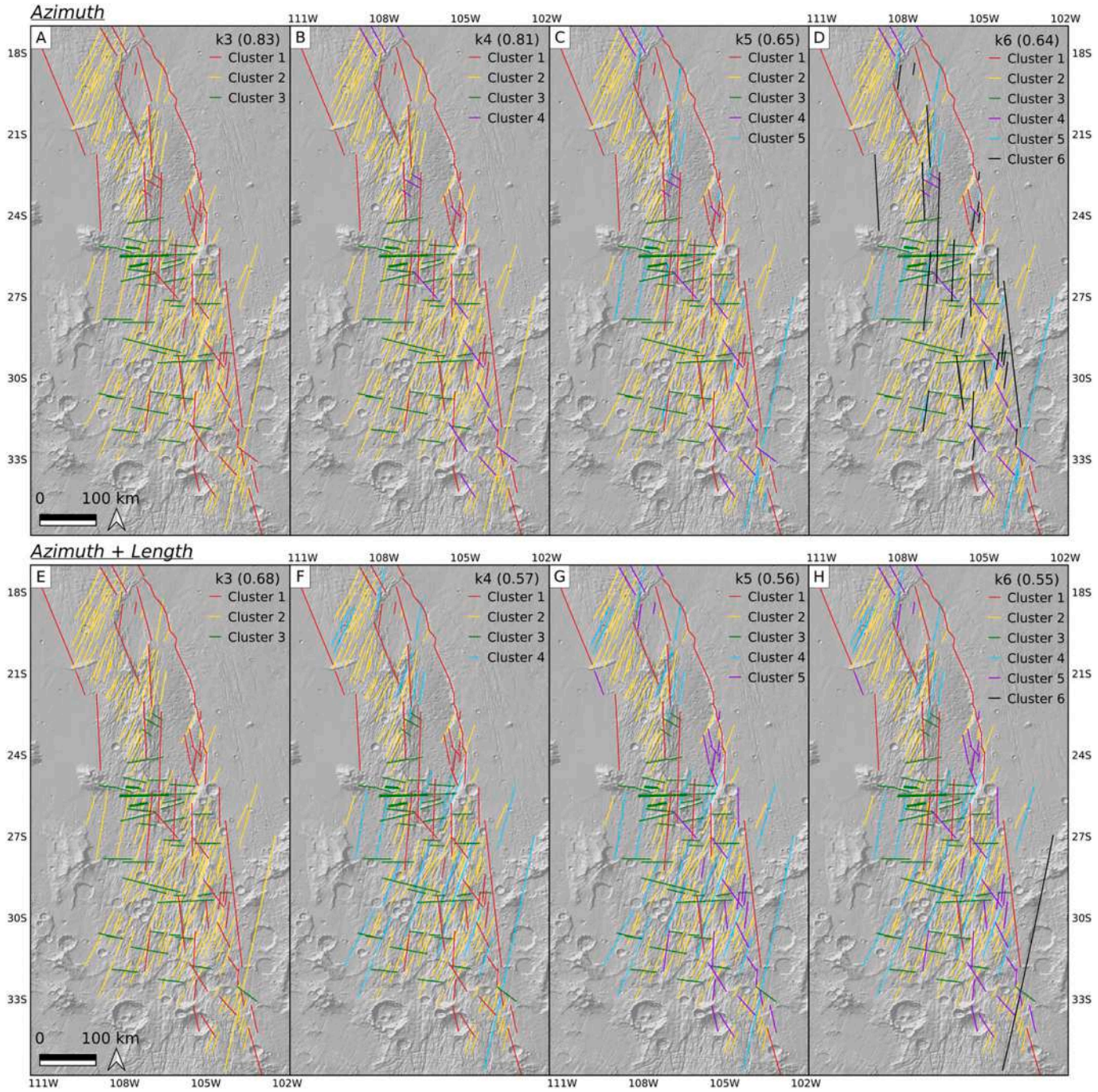

Fig. 3. Results of the cluster analysis considering (A-D) azimuth and (E-H) azimuth + length as attributes. A) k3: three clusters, average silhouette width for the entire dataset ($\bar{s}$): 0.83; B) k4: 4 clusters, $\bar{s}$: 0.81; C) k5: 5 clusters, $\bar{s}$: 0.65; D) k6: 6 clusters, $\bar{s}$: 0.64. E) k3: 3 clusters, $\bar{s}$: 0.68; F) k4: 4 clusters, $\bar{s}$: 0.57; G) k5: 5 clusters, $\bar{s}$: 0.56; H) k6: 6 clusters, $\bar{s}$: 0.55.

Table 1
Table shows the mean value and the standard deviation of the attributes of each cluster identified in the tests shown in Figs. 3 and 4.

Azimuth

Test	k3			k4				k5					k6					
Cluster	1	2	3	1	2	3	4	1	2	3	4	5	1	2	3	4	5	6
Counting	54	158	39	38	158	39	16	38	142	39	16	16	12	142	39	16	16	26
								azimuth (°)										
Mean	166	21	92	177	21	92	140	177	22	92	140	11	164	22	92	140	11	183
St. Dev.	20	5	8	10	5	8	11	10	4	8	11	1	4	4	8	11	1	5

Azimuth ± Length

Test	k3			k4				k5					k6					
Cluster	1	2	3	1	2	3	4	1	2	3	4	5	1	2	3	4	5	6
Counting	50	158	43	50	133	43	25	14	133	43	25	36	14	133	43	24	36	1
								Azimuth (°)										
Mean	170	21	95	170	21	95	18	172	21	95	18	168	172	21	95	18	168	*12*
St. Dev.	16	5	12	16	5	12	6	9	5	12	6	18	9	5	12	6	18	*0*
								Length (km)										
Mean	91	59	47	91	46	47	127	190	46	47	127	53	190	46	47	111	53	*518*
St. Dev.	82	47	27	82	15	27	84	97	15	27	84	21	97	15	27	27	21	*0*

Azimuth ± Length ± Centroid position

Test	k3			k4				k5					k6					
Cluster	1	2	3	1	2	3	4	1	2	3	4	5	1	2	3	4	5	6
Counting	52	135	64	52	96	64	39	52	96	61	39	3	26	96	61	39	3	26
								Azimuth (°)										
Mean	166	42	23	166	22	23	92	166	22	18	92	116	170	22	18	92	116	162
St. Dev.	20	32	27	20	5	27	8	20	5	5	8	74	15	5	5	8	74	24
								Length (km)										
Mean	75	55	72	75	58	72	48	75	58	54	92	437	106	58	54	92	437	43
St. Dev.	52	26	89	52	25	89	28	52	25	34	8	86	55	25	34	8	1	17
								Centroid position										
Mean	109	111	109	109	111	109	110	109	111	109	110	108	110	111	109	110	108	109
St. Dev.	1	1	1	1	1	1	1	1	1	1	1	0	1	1	1	1	0	1

2Azimuth ± Length ± Centroid position

Test	k3			k4				k5					k6					
Cluster	1	2	3	1	2	3	4	1	2	3	4	5	1	2	3	4	5	6
Counting	54	158	39	54	80	39	78	40	80	39	78	14	40	80	39	73	14	5
								Azimuth (°)										
Mean	166	21	92	166	23	92	19	176	23	92	19	138	176	23	92	20	138	11
St. Dev.	20	5	8	20	5	8	5	12	5	8	5	10	12	5	8	5	10	1
								Length (km)										
Mean	87	59	48	87	58	48	61	100	58	48	61	49	100	58	48	50	49	213
St. Dev.	80	47	28	80	21	28	63	89	21	28	63	17	89	21	28	30	17	154
								Centroid Position										
Mean	109	110	110	109	111	110	109	109	111	110	109	109	109	111	110	109	109	110
St. Dev.	1	1	1	1	1	1	1	1	1	1	1	1	1	1	1	1	1	1

Extended versions of the table are included in Appendix A.

Clusters 2 and 3 remain unchanged, whereas Cluster1-Azimuth-k3 divides into Cluster1-Azimuth-k4 and Cluster4-Azimuth-k4. These newly formed clusters contain 38 and 16 lineaments with average azimuths of 177° and 140°, respectively (Table 1). Fig. 3C, considering k = 5, shows Cluster2-Azimuth-k5, comprising 142 lineaments with an average azimuth of 22°, and Cluster5-Azimuth-k5, including 16 lineaments with an average azimuth of 11°, both emerging from the subdivision of Cluster2-Azimuth-k4. With k increased to 6 (Fig. 3D), Cluster1-Azimuth-k5 splits into Cluster1-Azimuth-k6 and Cluster6-Azimuth-k6, characterised by 12 and 26 lineaments, respectively, and mean azimuths of 164° and 183° (Table 1). In general, increasing k yields variations in the statistical parameters when one cluster splits into two. Specifically, the standard deviation (*sd*) and range decrease, indicating more selective grouping.

Fig. 3E-H illustrates the results of the clustering procedure using azimuth and length as attributes. In these tests, the average silhouette widths consistently exceed 0.5. Compared to Fig. 3A, the results obtained with Azimuth+Length-k3 (Fig. 3E) are largely similar, with minor differences in the number of lineaments in Clusters 1 and 3. This results in a marginal variation in the statistical parameters of the azimuth for both clusters. The mean lengths of each cluster are 91 km, 59 km and 47 km, respectively, but they exhibit a substantial range between the longest and shortest lineaments, along with considerable *sd* (Table 1 and Appendix A). As anticipated, both range and *sd* decrease with an increasing number of clusters. In contrast to the azimuth-only

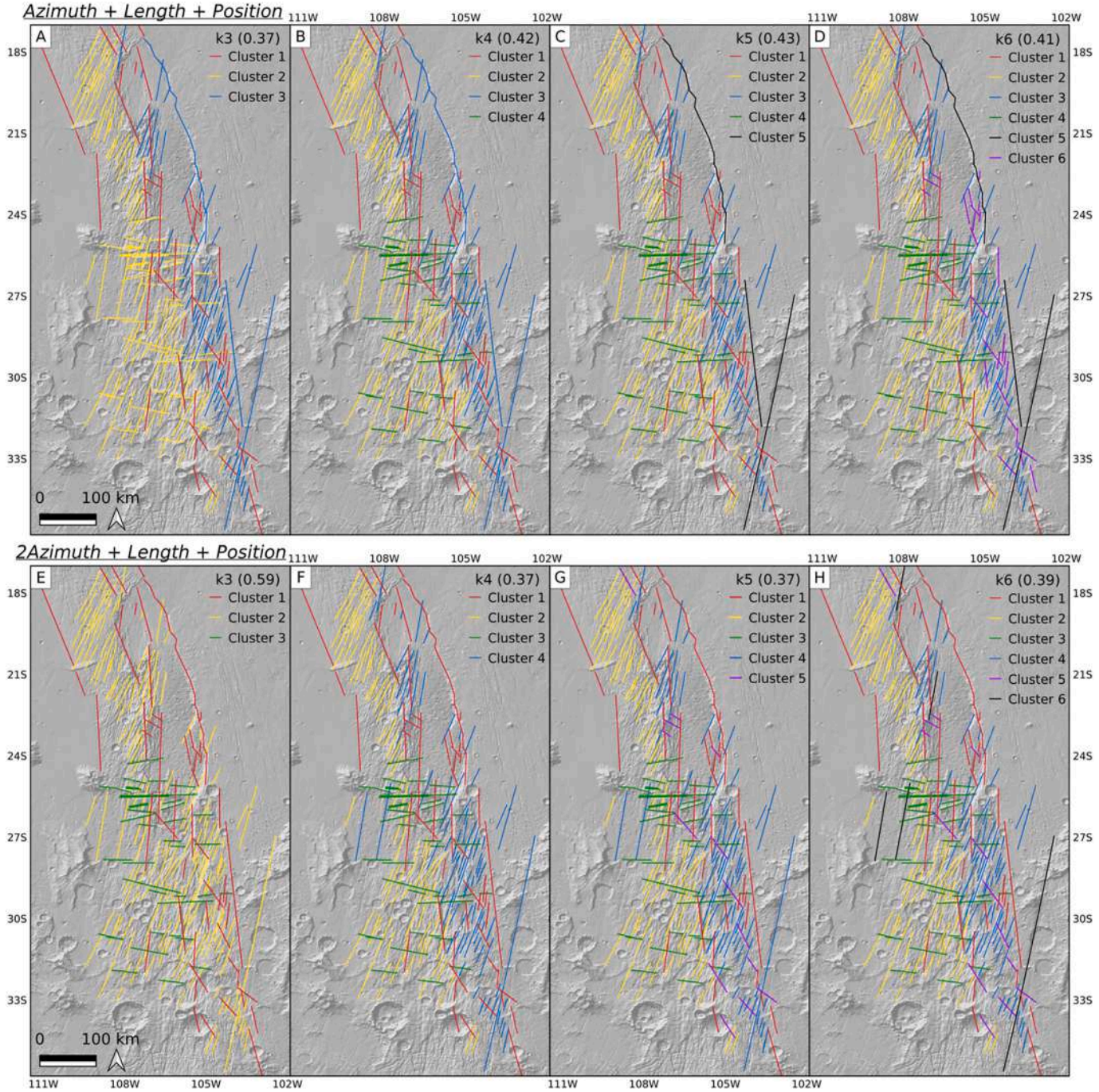

Fig. 4. Results of the clustering analysis considering as attributes (A-D) azimuth, length and position, and (*E*-H) azimuth, length and position weighting twice the azimuth. A) k3: three clusters, average silhouette width for the entire dataset ($\bar{s}$): 0.37; B) k4: 4 clusters, $\bar{s}$: 0.42; C) k5: 5 clusters, $\bar{s}$: 0.43; D) k6: 6 clusters, $\bar{s}$: 0.41; E) k3: three clusters, average silhouette width for the entire dataset ($\bar{s}$): 0.59; F) k4: four clusters, $\bar{s}$: 0.42; G) k5: 5 clusters, $\bar{s}$: 0.37; H) k6: 6 clusters, $\bar{s}$: 0.39.

test, with k = 4 (Fig. 3F), Cluster2-Azimuth+Length-k3 divides into Cluster2-Azimuth+Length-k4 and Cluster4-Azimuth+Length-k4. These new clusters contain lineaments with a mean azimuth difference smaller than their sd (mean azimuth: 21° and 18°; sd: 5° and 6° - Table 1) but are characterised by significantly different mean lengths: 46 km (sd: 15 km) for Cluster2-Azimuth+Length-k4 and 127 km (sd: 84 km) for Cluster4-Azimuth+Length-k4 (Table 1). Considering k = 5 (Fig. 3G), Cluster1-Azimuth+Length-k4 splits into two new clusters: Cluster1-Azimuth+Length-k5 and Cluster5-Azimuth+Length-k4. The latter comprises 36 lineaments with a mean azimuth of 168° and a mean length of 53 km, somewhat resembling Cluster4-Azimuth-k3, k4 and k5. Finally, results with k = 6 (Fig. 3H) reveal the new Cluster6-Azimuth+Length-k6, composed of a single lineament, which is the longest lineament previously included in Cluster2-Azimuth+Length-k3 and Cluster4-Azimuth+Length-k4, k5 (Table 1).

Results obtained by considering equally azimuth, length and position as attributes, and weighting of azimuth being twice that of length and position, are illustrated in Fig. 4A-D and E-H, respectively. In these tests, the average silhouette width values were lower than 0.5, except for the 2Azimuth + Length + Position-k3 test, which scored 0.59. A notable deviation from the Azimuth and Azimuth+Length tests is evident in Cluster 2 (yellow). Excluding 2Azimuth + Length + Position-k3 (Fig. 4E), which matches Azimuth-k3 (Fig. 3A) and is similar to Azimuth+Length-k3 (Fig. 3E), a distinct division of the yellow cluster into two separate clusters is observed (Clusters 2 and 3 in Fig. 4A-D and F-H) for all considered values of k. The newly formed Cluster 3 (blue) in both tests groups lineaments previously part of the yellow cluster located in the easternmost region of the study area. These lineaments are characterised by a mean azimuth ranging from 18° to 23° and a mean length of 50 km to 70 km, slightly differing from those in Cluster 2 (Table 1). Thus, the inclusion of position as an attribute significantly aids in distinguishing clusters of lineaments that are not discernible when only azimuth and length are considered. It should be noted that in the Azimuth+Length + Position-k5 analysis (Fig. 4C), the three longest mapped lineaments are grouped into a single cluster (i.e. Cluster 5-Azimuth+Length + Position-k5 and k6). In Fig. 4D, the Azimuth+Length + Position-k6 test also highlighted Cluster 6 (purple), whose azimuth and length values are nearly identical to those of Cluster 4-Azimuth-k4 to k6 and Cluster 5-Azimuth+Length-k5 and k6. A cluster with similar characteristics is also evident when the azimuth is weighted twice compared to length and position (Fig. 4G, H). In particular, the cluster subdivision observed in the 2Azimuth + Length + Position-k5 test closely resembles that of Azimuth-k4 (Fig. 3B), with the notable exception of the blue cluster.

In summary, the results obtained by considering only the azimuthal direction as an attribute are characterised by the highest values of the average silhouette width. The highest value, 0.83, is observed in *azimuth-k3*, a test that considers the fewest attributes (one) and the smallest number of clusters (three). Subsequently, the average silhouette width $\bar{s}$ slightly decreases by increasing the number of clusters and by adding new attributes. The lowest value of $\bar{s}$ is 0.37, occurs in the cases of *Azimuth + Length + Position-k3* and *2Azimuth + Length + Position-k4 and -k5*. The cluster analysis reveals that the azimuth-k3 (Fig. 3A) and 2*Azimuth + Length + Position-k3* (Fig. 4E) tests commonly exhibit the same subdivision into Cluster 1 (red, 54 lineaments NNW–SSE oriented), Cluster 2 (yellow, 158 lineaments NNE-SSW oriented) and Cluster 3 (green, 39 lineaments E-W oriented). The *Azimuth + Length-k3 test* (Fig. 3E) differs slightly from the aforementioned in terms of the number of lineaments grouped in Cluster 1 (50) and Cluster 3 (43) (Table 1). However, both clusters in *Azimuth + Length-k3* maintain the same orientation as those in *Azimuth-k3* and 2*Azimuth + Length + Position-k3*. In contrast, *Azimuth + Length + Position-k3* (Fig. 4A) does not reveal the E-W oriented, green cluster, which appears only from *Azimuth + Length + Position-k4* (Fig. 4B-D) onwards. In k3 tests, Cluster 3 is represented by a subgroup of the NNE-SSW oriented lineaments, located to the east of the study area. This subdivision persists in *Azimuth + Length + Position-k4*, *k5* and *k6* (Fig. 4B-D) and is also evident in 2*Azimuth + Length + Position-k4*, k5 *and* k6 (Fig. 4F-H).

In all tests, it can be observed that increasing *k*, results in the first three clusters identified in *k3s* splitting into new clusters. This indicates an increasingly refined subdivision of the dataset based on the considered attribute(s). This trend is evidenced by the decreasing sd and range of the considered attribute(s) as the number of clusters increases. For example, in the case of *Azimuth,* from *k4* to *k6* three additional preferential azimuthal directions emerge, leading to the subdivision of Cluster 1 and Cluster 2. Consequently, the *sd* of Cluster 1 decreases from 19.91° to 4.48° and the *sd* of Cluster 2 reduces from 5.39 to 4.49 (Table 1). However, as discussed in the next section, these new subdivisions do not always convey meaningful information or reliable geological scenarios. Therefore, the expertise of the operator in interpreting the geological significance of the results is crucial.

5. Discussion

5.1. Methodological consideration

In this work, cluster analysis was applied to tectonic lineaments outcropping in the CF area to classify them based on their azimuthal direction, length and position. Operationally, the application of the method necessitated two primary settings: i) selection of attributes for conducting the clustering analysis and ii) determination of the optimal number of clusters (*k)* to conclude the analysis. Results were found to be highly dependent on these settings, particularly the choice of attributes. This dependency was evident from the varying results obtained using different attribute combinations. For example, an analysis guided solely by azimuth (Fig. 3) resulted in clusters characterised by very low *sd* of the azimuth, regardless of the cluster count. In contrast, combining azimuth with length and position (Fig. 4) enabled the identification of clusters comprising lineaments at various distances from the main scarp of the CF, isolating the longest ones. In addition, the proposed procedure allows for differential weighting of one or more attributes compared to others. This step significantly influenced the cluster distribution, as demonstrated in Fig. 4, further highlighting the importance of attribute selection (and their weighting) in this clustering approach. Consequently, attribute selection should be guided by the analysis's objectives, the geological properties of the objects of the study and the most relevant geo-tectonic characteristics of the area under investigation. Here, the geological expertise of the operator plays a pivotal role and is indispensable.

The number of clusters (k) is another crucial parameter. The most objective method for determining the optimal value of k is to consider the average silhouette width $\bar{s}$. The greater the $\bar{s}$ is, the more robust the statistical results are (refer to the Materials and Methods Section for details). Kaufman and Rousseeuw (1990) suggested that the average silhouette width may serve as an a posteriori measure to evaluate the robustness of the chosen clustering structure in a trial-and-error approach. Therefore, the initial selection of k should be based on analysing the geological relevance of the resulting cluster distribution and its geological information. In our study, results indicated that $\bar{s}$ generally decreased with an increasing number of attributes and clusters, falling below 0.5 when all three attributes were considered alongside an increasing cluster count (Fig. 4A-D and E-H - excluding 2Azimuth + Length + Position-k3). These findings, while showing an $\bar{s}$ value below the threshold suggested by Kaufman and Rousseeuw (1990) for a reasonable clustering structure, revealed a previously unidentified subdivision of tectonic lineaments with significant geological implications, discussed later. Therefore, although the most robust results (i.e. those with the highest $\bar{s}$ values) were obtained considering only azimuth, clusters formed using all three attributes provided the most geological insight, as elaborated in the following paragraph.

5.2. Geological implications

Fig. 5 illustrates the sets of lineaments obtained through the geostatistical analysis of the azimuth performed by Balbi et al. (2024) (Fig. 5A) and the results of two clustering tests. The first one is the *Azimuth-k4* test (Fig. 5B) and the other one is the *2Azimuth + Length + Position-k5* test (Fig. 5C). For comparison, the same colours assigned to the four sets in Fig. 5A (red for *Set 1/Cluster 1*, yellow for *Set 2/Cluster 2*, green for *Set 3/Cluster 3* and purple for *Set 4/Cluster 4*) represent corresponding clusters. The clustering workflow was initially tested using the Azimuth as the solely attribute, resulting in a subdivision into four clusters (i.e. Azimuth-k4 test, Fig. 5B). The distribution of the clusters in the *Azimuth-k4* test aligns closely with that proposed in Fig. 5A. In particular, *Set3/Cluster3* and *Set4/Cluster4* perfectly match in terms of both number of grouped lineaments and mean azimuth value. Although *Set1/Cluster1* and *Set2/Cluster2* show minor variations in the number of grouped lineaments, differences in mean azimuth remain below the *sd*. These results highlight the proposed clustering workflow's ability to replicate results from classical geostatistical methods. Furthermore, the identification of four azimuthal sets of tectonic lineaments through both methods reinforces their reliability and the tectonic interpretation within the evolutionary model shown in Fig. 6. This model, proposed for the present-day setting of the CF (Balbi et al., 2024), features the sets/clusters in a Riedel shear model, consistent with a model of strain partitioning and shear fracture orientation (Riedel, 1929; Swanson, 1988; Storti et al., 2006; Fossen, 2016). Their spatial distribution and angular relationships suggest development within a NNW–SSE oriented right-lateral strike-slip deformation corridor, where the sets/clusters represent: *Set1/Cluster1* (red in Fig. 6) as the main shear zone; *Set2/Cluster2* (yellow) as R-shear structures; *Set3/Cluster3* (green) as T-Structures; *Set4/Cluster4* (purple) as P-shear structures (Fig. 6). The angles between sets exceed those expected in a classical Riedel shear model, indicating an extensional component to the kinematics. This aligns with the proposed existence of a crustal-scale, listric normal fault responsible for forming the longitudinal, regional half-graben morphology.

When considering the three attributes together with twice the weight for azimuth and using five clusters (k = 5) (Fig. 5C), new tectonic insights on the CF can be derived. *Set2/Cluster2-Azimuth-k4* (Fig. 5A/B) is divided into two subpopulations. These include *Cluster2-2Azimuth-Length-Position-k5* (yellow in Fig. 5C) and *Cluster4-2Azimuth-Length-Position-k5* (blue in Fig. 5C). The differences in mean azimuth and length between these two clusters are smaller than the *sd*. This resulted in the non-recognition of this subdivision when using only azimuth and length as attributes or employing classical geostatistical methods. The positions of the lineaments are the discriminating factor for these clusters, as they are situated at varying distances from the main scarp of the CF. Specifically, *Cluster2-2Azimuth-Length-Position-k5* (yellow) is more distant, while *Cluster4-2Azimuth-Length-Position-k5* (blue) is closer. As discussed in the introduction, various authors consider the main scarp of the CF as the superficial manifestation of a crustal-scale fault (e.g. Hauber and Kronberg, 2005; Montgomery et al., 2009; Balbi et al., 2024). Consequently, the lineaments within these clusters may relate to their formation at different distances from the main fault zone of the CF. We confirmed the geological significance of this division by calculating the Length-Spacing ratio (L/S). The L/S ratio, a scale-independent nondimensional parameter, involves the length (L) of the structure and its perpendicular distance or spacing (S) to an adjacent, nearly parallel structure of the same population. This ratio reflects the nucleation of new faults/fractures between two pre-existing ones, indicating fracture infilling in evolving brittle deformation conditions (Lachenbruch, 1961;

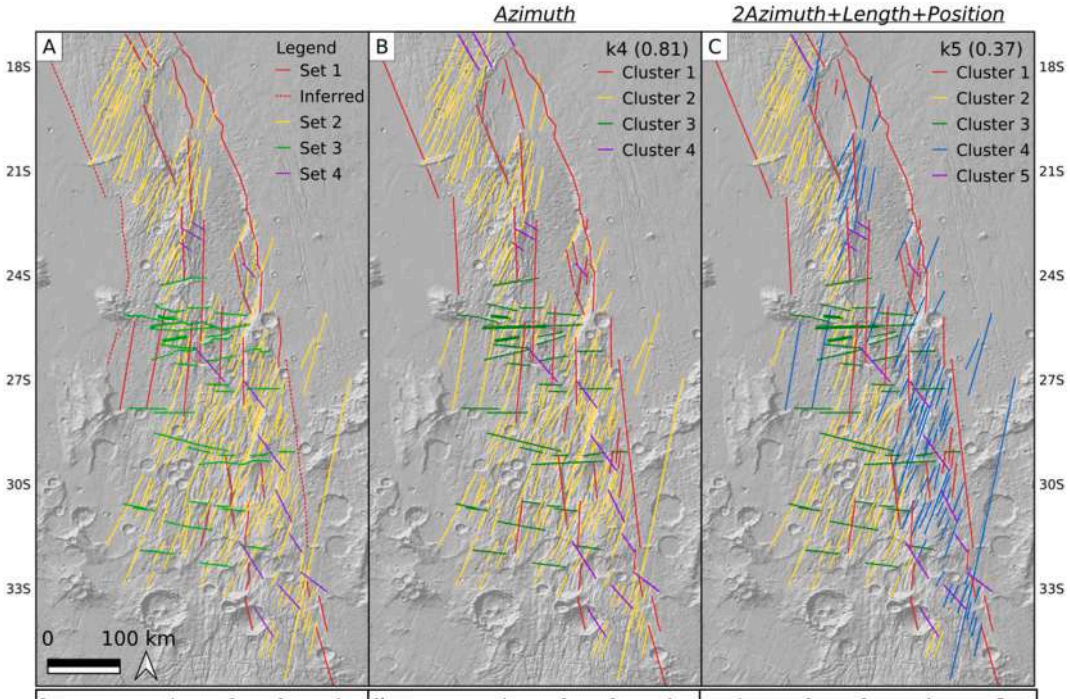

Set	1	2	3	4
Counting	32	167	39	13
Mean azimuth (sd)	172° (13°)	20° (6°)	92° (8°)	140° (10°)
Mean Length (km)	125	55	48	48

Cluster	1	2	3	4
Counting	38	158	39	16
Mean azimuth (sd)	177° (10°)	21° (5°)	92° (8°)	140° (11°)
Mean Length (km)	99	59	48	55

1	2	3	4	5
40	80	39	78	14
176 ° (12°)	23° (5°)	92 (8°)	19° (5°)	138° (10°)
99	57	48	60	49

Fig. 5. Comparison among A) sets of lineaments obtained through the geostatistical analysis of the azimuth (Balbi et al., 2024), and clusters obtained in this study through B) Azimuth-k4 and C) 2Azimuth + Length + Position-k5 tests. Distribution of sets/clusters in A and B is substantially identical. C shows a new subdivision of Set2 in two subpopulations (Cluster2, yellow and Cluster 4, blue) spatially separated. (For interpretation of the references to colour in this figure legend, the reader is referred to the web version of this article.)

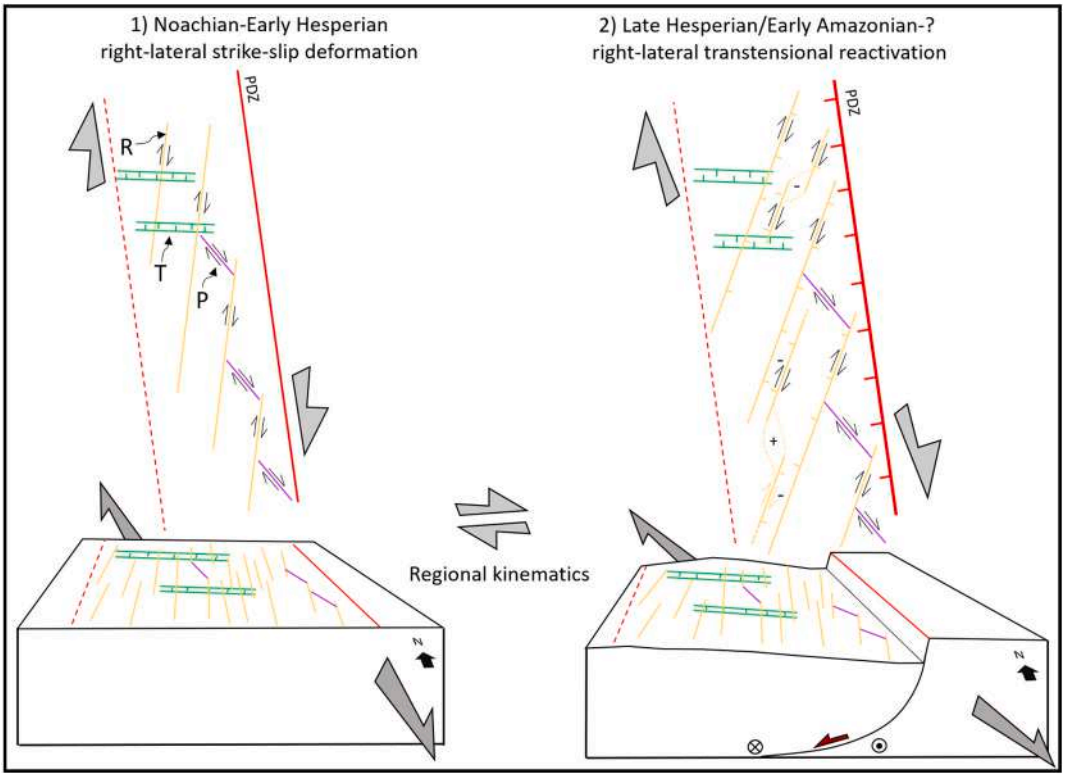

Fig. 6. Polyphase tectonic model proposed for the CF consisting of 1) Noachian to Early Hesperian right-lateral strike-slip deformation (PDZ: Principal Displacement Zone) and 2) Late Hesperian/Early Amazonian-? right-lateral transtensional reactivation (modified from Balbi et al., 2024).

Durney and Kisch, 1994; Bai and Pollard, 2000; Bai et al., 2000; Tavani et al., 2006). In addition, L/S is used to determine the spatial frequency of lineaments resulting from crustal tectonic stresses, indicative of the intensity of brittle deformation (Cianfarra and Salvini, 2016; Rossi et al., 2018, 2020; Cianfarra et al., 2022). In general, L/S is proportional to the intensity of brittle deformation. Therefore, for populations of faults or fractures developed in fault zones, L/S decreases with distance from the fault zone. For instance, areas with intense deformation exhibit closely spaced fractures/faults, leading to higher L/S values than low-deformed areas. In our study, the L/S ratios for Cluster2-2Azimuth-Length-Position-k5 and Cluster4-2Azimuth-Length-Position-k5 are 3.33 and 3.53, respectively. This significant difference between the clusters reflects their proximity to the main scarp of the CF; therefore, the main fault zone. It demonstrates the importance of attribute selection in cluster analysis for categorising tectonic lineaments.

It is noteworthy that the spatial distribution of *Cluster4-2Azimuth-Length-Position-k5* is not uniform. In the northern part of the study area, the number of lineaments belonging to this cluster is drastically lower than in the south, affecting the overall L/S ratio. When calculated solely in the southernmost part of the CF, where both clusters are uniformly distributed, the L/S ratio for *Cluster2-2Azimuth-Length-Position-k5* (2.83) remains lower than that of *Cluster4-2Azimuth-Length-Position-k5* (3.49). Consequently, the subdivision presented in Fig. 5C suggests that i) at least two areas with varying degrees of brittle deformation exist and ii) deformation decreases westward, increasing with distance from the main scarp of the CF, which likely represents the focal point of deformation. A crustal-scale fault zone such as the CF could serve as a conduit for magma and fluid migration. The eastward increase in brittle deformation may enhance secondary permeability near the main scarp of the CF. Therefore, in the event of volcanic activity, more superficial manifestations can be anticipated in the region corresponding to *Cluster4-2Azimuth-Length-Position-k5*. This is of particular interest when considering the distribution of mounds (i.e. positive topographic landforms) possibly related to volcanic origin identified by Pieterek et al. (2024) in the central part of the CF. These mounds are more numerous and closely spaced near the main scarp of the CF, aligning with the area influenced by *Cluster4-2Azimuth-Length-Position-k5*.

The spatial distribution of clusters also implies temporal considerations. Specifically, the different spatial distribution of lineaments belonging to *Cluster4-2Azimuth-Length-Position-k5* (depicted in blue in Fig. 5C) marks the transition between the middle Noachian terrains and the Late Hesperian lavas, as shown in Fig. 7A-C. In general, the majority of lineaments in both *Cluster2-2Azimuth-Length-Position-k5* and *Cluster4-2Azimuth-Length-Position-k5* are located in Late-Middle Noachian terrains. This distribution suggests that these clusters formed prior to the emplacement of the Late Hesperian lavas. This inference extends to lineaments in *Cluster3-2Azimuth-Length-Position-k5* and, to some extent, *Cluster1-2Azimuth-Length-Position-k5*. Notably, *Cluster1-2Azimuth-Length-Position-k5* (aligned parallel to the principal displacement zone in the proposed tectonic evolutionary model in Fig. 6) includes lineaments marking the lithological contact between Noachian and Hesperian terrains in the west, and the main scarp of the CF. The latter cuts and offsets the Hesperian lava flows indicating a reactivation of the main fault zone of the CF and of some of the identified sets/clusters after the Late Hesperian lava flows were emplaced.

The results of the clustering analysis support the hypothesis of a polyphase tectonic history characterised by a Noachian right-lateral strike-slip event followed by a Late Hesperian/Early Amazonian transtensional reactivation. These temporal constraints are in agreement with evaluations proposed in the literature regarding the tectonics of the CF related to Tharsis' deformation (Tanaka and Davis, 1988; Tanaka et al., 1991; Dohm et al., 2001; Anderson et al., 2001; Hauber and Kronberg, 2005; Montgomery et al., 2009; Smith et al., 2009; Bouley et al., 2018; Andrews-Hanna & Broquet, 2023; Pieterek et al., 2024).

6. Conclusions

The proposed clustering workflow is a valuable tool for classifying

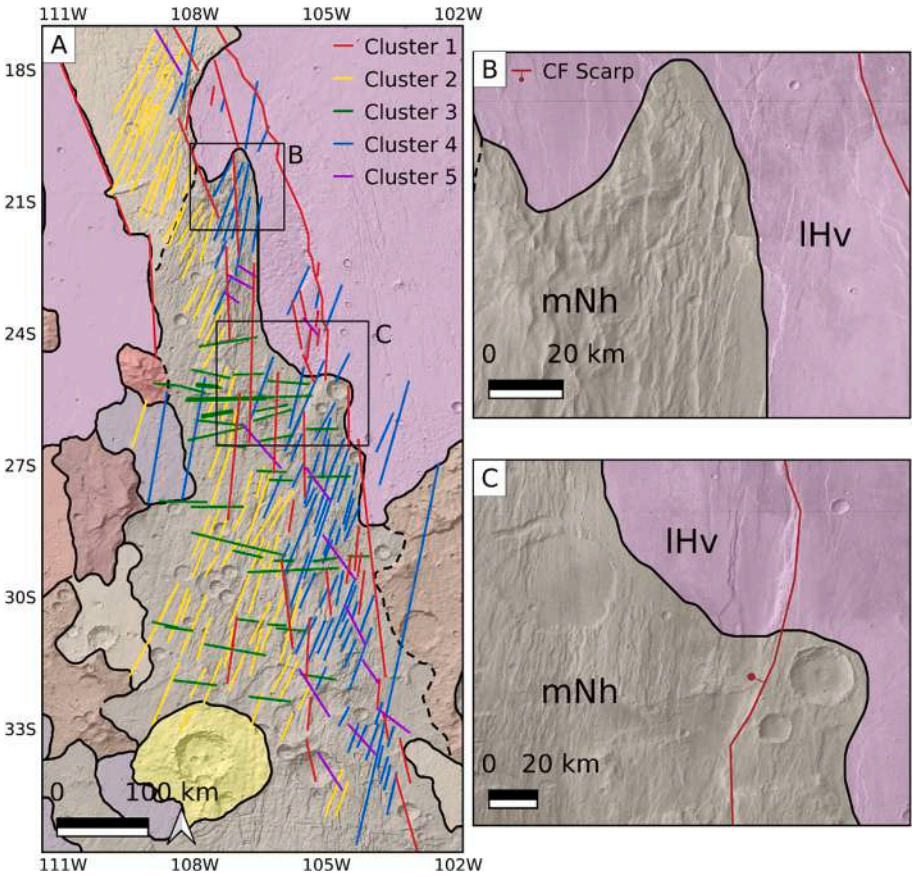

Fig. 7. A) Sketch map showing the position of the clusters derived from the 2Azimuth-Length-Position-k5 test with respect to the geologic units from Tanaka et al. (2014). Clusters mainly affect late to middle Noachian terrains (mNh). B) and C) show Late Hesperian lavas (lHv) that superimpose lineaments belonging to all clusters and the main scarp of the CF (belonging to cluster 1) that cuts and offsets lHv. These temporal constraints agree with the polyphase tectonic scenario shown in Fig. 6.

elements based on their characteristics by reducing the interpreter bias. This approach is particularly beneficial when managing complex databases containing hundreds or thousands of elements, such as tectonic lineaments in our study, each with numerous attributes. The method has been extremely effective in examining complex, tectonically controlled regions including the CF on Mars. Cluster analysis has demonstrated its capability to both replicate results obtained by classic geostatistical methods and identify previously unrecognised areas characterised by varying intensities of deformation, yielding significant tectonic and geological insights.

The cluster analysis is guided by two crucial parameters: the attributes used for grouping objects and the optimal number of clusters from a geological perspective. The selection of attributes is a systematic choice driven by the aim of the analysis and scale/resolution at which it is conducted. For this study, the goal of revealing the regional-scale tectonics at the CF necessitated focusing on characteristics of the mapped lineaments representative of regional/crustal deformation (e.g. orientation, length, position) rather than factors related to local-scale phenomena (e.g. morphometric characteristics). Another challenging aspect is determining the optimal number of clusters. The Silhouette index can be employed to assess the statistical consistency of the clustering results. However, the final decision on concluding the analysis rests with the operator, who must validate the geological reliability of the cluster distributions. Thus, both aspects crucially rely on the fundamental role of the operator, whose geological expertise is essential in guiding and conducting the analysis and cannot be neglected in favour of a purely objective procedure.

When the attributes to be used and the number of clusters are adequately tuned, the proposed clustering workflow proves to be a useful tool for providing new insights into the analysis of tectonic lineaments in complex areas such as the CF. In this study, considering all available attributes, the cluster analysis successfully identifies groups of tectonic lineaments whose distribution is extremely useful for recognising different deformation conditions and unravelling the geo-tectonic model of the CF.

The performance of the proposed workflow is promising. As a future perspective, it will be applied to more complex areas characterised by a higher number of tectonic lineaments (likely thousands or tens of thousands), such as the Noctis Labyrinthus and the entire Tharsis Dome. Here, grouping tectonic lineaments based on their characteristics (e.g. orientation, length and position) could be extremely challenging and subject to subjective interpretations. On the other hand, the efficiency of the proposed method will be tested in local scale analyses as well where new parameters, such as morphometric characteristics (e.g. sinuosity, fault displacement, slope) will be considered.

CRediT authorship contribution statement

Evandro Balbi: Writing – review & editing, Writing – original draft, Visualization, Software, Methodology, Investigation, Data curation, Conceptualization. **Paola Cianfarra:** Writing – review & editing, Visualization, Validation, Conceptualization. **Laura Crispini:** Writing – review & editing, Validation, Supervision, Conceptualization. **Silvano Tosi:** Writing – review & editing, Validation, Conceptualization. **Gabriele Ferretti:** Writing – original draft, Visualization, Validation, Supervision, Software, Methodology, Investigation, Data curation, Conceptualization.

Declaration of competing interest

The authors declare no known competing of interest.

Data availability

Data will be made available on request.

Acknowledgment

The authors would like to acknowledge Dr. Filippo Carboni and the anonymous reviewer whose comments and suggestions certainly improved the manuscript. We also acknowledge the open-source software QGIS 3.18_Zurich and the R packages used for the clustering workflow. E.B. acknowledge the Department of Earth, Life and Environmental Science (DISTAV) of the University of Genova for the financial and material support provided in the context of his PhD program within the XXXVI cycle.

Appendix A

In the following tables the statistical parameters of the clusters identified through the different tests performed (i.e. considering different combination of attributes and different number of clusters *k*) are shown in detail.

Table A1
Statistical parameter of clusters identified through the azimuth alone test.

Test	k3			k4				k5					k6					
Cluster	1	2	3	1	2	3	4	1	2	3	4	5	1	2	3	4	5	6
Counting	54	158	39	38	158	39	16	38	142	39	16	16	12	142	39	16	16	26
								azimuth (°)										
Max	189	33	104	189	33	104	153	189	33	104	153	13	171	33	104	153	13	189
Min	119	10	74	158	10	74	119	158	13	74	119	10	158	13	74	119	10	173
Range	70	23	31	32	23	31	34	32	19	31	34	3	13	19	31	34	3	16
Mean	166	21	92	177	21	92	140	177	22	92	140	11	164	22	92	140	11	183
Median	170	22	92	180	22	92	143	180	22	92	143	11	164	22	92	143	11	185
St. Dev.	20	5	8	10	5	8	11	10	4	8	11	1	4	4	8	11	1	5

Table A2
Statistical parameter of clusters identified through the azimuth and length test.

Test	k3			k4				k5					k6					
Cluster	1	2	3	1	2	3	4	1	2	3	4	5	1	2	3	4	5	6
Counting	50	158	43	50	133	43	25	14	133	43	25	36	14	133	43	24	36	1
								Azimuth (°)										
Max	189	33	127	189	33	127	28	185	33	127	28	189	185	33	127	28	189	*12*
Min	138	10	74	138	10	74	10	158	10	74	10	138	158	10	74	10	138	*12*
Range	51	23	53	51	22	53	18	28	22	53	18	51	28	22	53	18	51	*0*
Mean	170	21	95	170	21	95	18	172	21	95	18	168	172	21	95	18	168	*12*
Median	173	22	94	173	22	94	20	175	22	94	20	170	175	22	94	20	170	*12*
St. Dev.	16	5	12	16	5	12	6	9	5	12	6	18	9	5	12	6	18	*0*
								Length (km)										
Max	474	518	156	474	80	156	518	474	80	156	518	103	474	80	156	179	103	*518*
Min	17	17	20	17	17	20	72	113	17	20	72	17	113	17	20	72	17	*518*
Range	458	501	136	458	63	136	446	362	63	136	446	87	362	63	136	107	87	*0*
Mean	91	59	47	91	46	47	127	190	46	47	127	53	190	46	47	111	53	*518*
Median	59	50	38	59	48	38	106	153	48	38	106	53	153	48	38	106	53	*518*
St. Dev.	82	47	27	82	15	27	84	97	15	27	84	21	97	15	27	27	21	*0*

Cluster6-k6 includes an insufficient number of lineaments for a reliable statistical analysis of the attributes.

Table A3
Statistical parameter of clusters identified through the azimuth, length and position test.

Test	k3			k4				k5					k6					
Cluster	1	2	3	1	2	3	4	1	2	3	4	5	1	2	3	4	5	6
Counting	52	135	64	52	96	64	39	52	96	61	39	3	26	96	61	39	3	26

(*continued on next page*)

Table A3 (*continued*)

Test	k3			k4				k5					k6					
Cluster	1	2	3	1	2	3	4	1	2	3	4	5	1	2	3	4	5	6
								Azimuth (°)										
Max	189	104	173	189	33	173	104	189	33	29	104	173	189	33	29	104	173	189
Min.	119	10	10	119	10	10	74	119	10	10	74	12	139	10	10	74	12	119
Range	70	95	164	70	23	164	31	70	23	19	31	161	50	23	19	31	161	70
Mean	166	42	23	166	22	23	92	166	22	18	92	116	170	22	18	92	116	162
Median	170	25	19	170	23	19	92	170	23	19	92	163	175	23	19	92	163	168
St. Dev.	20	32	27	20	5	27	8	20	5	5	8	74	15	5	5	8	74	24
								Length (km)										
Max	240	165	518	240	165	518	156	240	165	179	104	518	240	165	179	104	518	85
Min	17	20	17	17	22	17	20	17	22	17	74	318	24	22	17	74	318	17
Range	223	145	501	223	144	501	136	223	144	162	31	201	216	144	162	31	201	69
Mean	75	55	72	75	58	72	48	75	58	54	92	437	106	58	54	92	437	43
Median	57	50	47	57	54	47	38	57	54	45	92	474	100	54	45	92	474	39
St. Dev.	52	26	89	52	25	89	28	52	25	34	8	86	55	25	34	8	1	17
								Centroid position										
Max	112	113	109	112	113	109	113	112	113	109	113	108	112	113	109	113	108	110
Min	108	108	107	108	109	107	108	108	109	107	108	108	109	109	107	108	108	108
Range	5	5	3	5	4	3	5	5	4	3	5	0	3	4	3	5	0	2
Mean	109	111	109	109	111	109	110	109	111	109	110	108	110	111	109	110	108	109
Median	109	111	109	109	111	109	110	109	111	109	110	108	110	111	109	110	108	109
St. Dev.	1	1	1	1	1	1	1	1	1	1	1	0	1	1	1	1	0	1

Cluster5-k5 and -k6 include an insufficient number of lineaments for reliable statistical analysis of the attributes.

Table A4
Statistical parameter of clusters identified through the azimuth, length and position test weighting twice the azimuth compared to the other attributes.

Test	k3			k4				k5					k6					
Cluster	1	2	3	1	2	3	4	1	2	3	4	5	1	2	3	4	5	6
Counting	54	158	39	54	80	39	78	40	80	39	78	14	40	80	39	73	14	5
								Azimuth (°)										
Max	189	33	104	189	33	104	29	189	33	104	29	153	189	33	104	29	153	12
Min	119	10	74	119	12	74	10	151	12	74	10	119	151	12	74	10	119	10
Range	70	23	31	70	21	31	19	38	21	31	19	34	38	21	31	19	34	3
Mean	166	21	92	166	23	92	19	176	23	92	19	138	176	23	92	20	138	11
Median	170	22	92	170	23	92	20	179	23	92	20	141	179	23	92	20	141	10
St. Dev.	20	5	8	20	5	8	5	12	5	8	5	10	12	5	8	5	10	1
								Length (km)										
Max	474	518	156	474	134	156	518	474	134	156	518	74	474	134	156	179	74	518
Min	17	17	20	17	22	20	17	17	22	20	17	22	17	22	20	17	22	105
Range	458	501	136	458	112	136	501	458	112	136	501	52	458	112	136	162	52	413
Mean	87	59	48	87	58	48	61	100	58	48	61	49	100	58	48	50	49	213
Median	59	50	38	59	56	38	47	61	56	38	47	51	61	56	38	45	51	150
St. Dev.	80	47	28	80	21	28	63	89	21	28	63	17	89	21	28	30	17	154
								Centroid Position										
Max	112	113	113	112	113	113	112	112	113	113	112	110	112	113	113	110	110	112
Min	108	107	108	108	110	108	107	108	110	108	107	108	108	110	108	107	108	108
Range	5	7	5	5	4	5	5	5	4	5	5	2	5	4	5	3	2	4
Mean	109	110	110	109	111	110	109	109	111	110	109	109	109	111	110	109	109	110
Median	109	110	110	109	111	110	109	109	111	110	109	109	109	111	110	109	109	109
St. Dev.	1	1	1	1	1	1	1	1	1	1	1	1	1	1	1	1	1	1

Cluster6-k6 included an insufficient number of lineaments for reliable statistical analysis of the attributes.

References

Aghaee, A., Shamsipour, P., Hood, S., Haugaard, R., 2021. A convolutional neural network for semi-automated lineament detection and vectorisation of remote sensing data using probabilistic clustering: a method and a challenge. Comput. Geosci. 151, 104724 https://doi.org/10.1016/j.cageo.2021.104724.

Anderson, R.C., Dohm, J.M., Golombek, M.P., Haldemann, A.F.C., Franklin, B.J., Tanaka, K.L., Lias, J., Peer, B., 2001. Primary centers and secondary concentrations of tectonic activity through time in the western hemisphere of Mars. J. Geophys. Res. Planets 106, 20563–20585. https://doi.org/10.1029/2000JE001278.

Anderson, R.C., Dohm, J.M., Williams, J.P., Robbins, S.J., Siwabessy, A., Golombek, M. P., Schroeder, J.F., 2019. Unraveling the geologic and tectonic history of the Memnonia-Sirenum region of Mars: implications on the early formation of the Tharsis rise. Icarus 332, 132–150. https://doi.org/10.1016/j.icarus.2019.06.010.

Andrews-Hanna, J.C., Broquet, A., 2023. The history of global strain and geodynamics on Mars. Icarus 395, 115476.

Anguita, F., Farelo, A.F., López, V., Mas, C., Muñoz-Espadas, M.J., Márquez, Á., Ruiz, J., 2001. Tharsis dome, Mars: new evidence for Noachian-Hesperian thick-skin and Amazonian thin-skin tectonics. J. Geophys. Res. 106 (E4), 7577–7589. https://doi.org/10.1029/2000JE001246.

Ansari, A., Noorzad, A., Zafarani, H., 2009. Clustering analysis of the seismic catalog of Iran. Comput. Geosci. 35 (3), 475–486. https://doi.org/10.1016/j.cageo.2008.01.010.
Arabie, P., Hubert, L., De Soete, G., Gordon, A., 1996. Hierarchical classification. In: Arabie, P., Hubert, L., De Soete, G., Gordon, A. (Eds.), Clustering and Classification, pp. 65–121.
Bai, T., Pollard, D.D., 2000. Closely spaced fractures in layered rocks: initiation mechanism and propagation kinematics. J. Struct. Geol. 22 (10), 1409–1425. https://doi.org/10.1016/S0191-8141(00)00062-6.
Bai, T., Pollard, D.D., Gao, H., 2000. Explanation for fracture spacing in layered materials. Nature 403 (6771), 753–756. https://doi.org/10.1038/35001550.
Balbi, E., Marini, F., 2024. Lineament domain analysis to unravel tectonic settings on planetary surfaces: insights from the Claritas fossae (Mars). Geosciences 14 (3), 79.
Balbi, E., Cianfarra, P., Ferretti, G., Crispini, L., Tosi, S., 2022. The Claritas Fossae Region, an Example of Polyphasic Deformation on Mars?, 16 https://doi.org/10.5194/epsc2022-1041, 2022–1041.
Balbi, E., Ferretti, G., Tosi, S., Crispini, L., Cianfarra, P., 2024. Polyphase tectonics on Mars: insight from the Claritas fossae. Icarus 411, 115972. https://doi.org/10.1016/j.icarus.2024.115972.
Bouley, S., Baratoux, D., Paulien, N., Missenard, Y., Saint-Bézar, B., 2018. The revised tectonic history of Tharsis. Earth Planet. Sci. Lett. 488, 126–133. https://doi.org/10.1016/j.epsl.2018.02.019.
Carr, M.H., Head III, J.W., 2010. Geologic history of Mars. Earth Planet. Sci. Lett. 294 (3–4), 185–203. https://doi.org/10.1016/j.epsl.2009.06.042.
Ceccato, A., Tartaglia, G., Antonellini, M., Viola, G., 2022. Multiscale lineament analysis and permeability heterogeneity of fractured crystalline basement blocks. Solid Earth 13 (9), 1431–1453. https://doi.org/10.5194/se-13-1431-2022.
Christensen, P.R., Jakosky, B.M., Kieffer, H.H., Malin, M.C., Mcsween, H.Y., Nealson, K., Mehall, G.L., Silverman, S.H., Ferry, S., Caplinger, M., Ravine, M., 2004. The thermal emission imaging system (Themis) for the Mars 2001 odyssey mission. Space Sci. Rev. 110, 85–130. https://doi.org/10.1023/B:SPAC.0000021008.16305.94.
Cianfarra, P., Salvini, F., 2014. Ice sheet surface lineaments as nonconventional indicators of East Antarctica bedrock tectonics. Geosphere 10 (6), 1411–1418. https://doi.org/10.1130/GES01074.1.
Cianfarra, P., Salvini, F., 2016. Quantification of fracturing within fault damage zones affecting late Proterozoic carbonates in Svalbard. Rendiconti Lincei 27, 229–241. https://doi.org/10.1007/s12210-016-0527-5.
Cianfarra, P., Locatelli, M., Capponi, G., Crispini, L., Rossi, C., Salvini, F., Federico, L., 2022. Multiple reactivations of the Rennick graben fault system (northern Victoria land, Antarctica): new evidence from paleostress analysis. Tectonics 41 (6). https://doi.org/10.1029/2021TC007124 e2021TC007124.
Cianfarra, P., Morelli, D., Salvini, F., 2024. Geostatistical analysis of lineament domains: the study case of the Apennine Seismic Province of Italy. Geosciences 14 (5), 131. https://doi.org/10.3390/geosciences14050131.
Davey, S.C., Ernst, R.E., Samson, C., Grosfils, E.B., 2013. Hierarchical clustering of pit crater chains on Venus. Can. J. Earth Sci. 50 (1), 109–126. https://doi.org/10.1139/cjes-2012-0054.
de Arruda Passos, V.S., de Miranda, T.S., Oliveira, J.T.C., Celestino, M.A.L., Corrêa, R., Topan, J.G., da Cruz Falcão, T., 2022. Quantification of the spatial arrangement of structural lineaments and deformation bands: implications for the tectonic evolution of the eastern border of the Araripe Basin, NE Brazil. J. S. Am. Earth Sci. 118, 103934 https://doi.org/10.1016/j.jsames.2022.103934.
Dohm, James M., Tanaka, K.L., 1999. Geology of the Thaumasia region, Mars: plateau development, valley origins, and magmatic evolution. Planet. Space Sci. 47, 411–431. https://doi.org/10.1016/S0032-0633(98)00141-X.
Dohm, J.M., Tanaka, K.L., Hare, T.M., 2001. Geologic Map of the Thaumasia Region, Mars: U.S. Geological Survey Geologic Investigations Series I–2650, 3 Sheets. https://pubs.usgs.gov/imap/i2650/.
Dohm, J.M., Spagnuolo, M.G., Williams, J.P., Viviano-Beck, C.E., Karunatillake, S., Álvarez, O., Maruyama, S., 2015. The Mars plate-tectonic-basement hypothesis. In: Lunar and Planetary Science Conference (p. 1741). https://www.hou.usra.edu/meetings/lpsc2015/pdf/1741.pdf.
Dohm, J.M., Maruyama, S., Kido, M., Baker, V.R., 2018. A possible anorthositic continent of early Mars and the role of planetary size for the inception of earth-like life. Geosci. Front. 9, 1085–1098. https://doi.org/10.1016/j.gsf.2016.12.003.
Drury, S.A., 2004. Image Interpretation in Geology.
Durney, D.W., Kisch, H.J., 1994. A field classification and intensity scale for first-generation cleavages. AGSO J. Aust. Geol. Geophys. 15 (3), 257–295.
Duxbury, T.C., Kirk, R.L., Archinal, B.A., Neumann, G.A., 2002. Mars geodesy/cartography working group recommendations on Mars cartographic constants and coordinate systems. Int. Arch. Photogramm. Remote. Sens. Spat. Inf. Sci. 34 (4), 743–748.
Edwards, C.S., Nowicki, K.J., Christensen, P.R., Hill, J., Gorelick, N., Murray, K., 2011. Mosaicking of global planetary image datasets: 1. Techniques and data processing for thermal emission imaging system (THEMIS) multi-spectral data. J. Geophys. Res. Planets 116. https://doi.org/10.1029/2010JE003755.
Faraj, F., Ortiz, J.M., 2021. A simple unsupervised classification workflow for defining geological domains using multivariate data. Min. Metall. Explor. 38 (3), 1609–1623. https://doi.org/10.1007/s42461-021-00428-5.
Fergason, R.L., Hare, T.M., Laura, J., 2018. HRSC and MOLA Blended Digital Elevation Model at 200m v2. Astrogeology PDS Annex, U.S. Geological Survey. http://bit.ly/HRSC_MOLA_Blend_v0.
Fossen, H., 2016. Structural Geology. Cambridge University Press.
Franceschini, Z., Cioni, R., Scaillet, S., Corti, G., Sani, F., Isola, I., Brune, S., 2020. Recent volcano-tectonic activity of the Ririba rift and the evolution of rifting in South Ethiopia. J. Volcanol. Geotherm. Res. 403, 106989 https://doi.org/10.1016/j.jvolgeores.2020.106989.
Golombek, M.P., Bridges, N.T., 2000. Erosion rates on Mars and implications for climate change: constraints from the pathfinder landing site. J. Geophys. Res. 105 (E1), 1841–1853. https://doi.org/10.1029/1999JE001043.
Golombek, M.P., Phillips, R.J., 2010. Mars tectonics. Planet. Tecton. 11, 183–232.
Golombek, M.P., Grant, J.A., Crumpler, L.S., Greeley, R., Arvidson, R.E., Bell III, J.F., Squyres, S.W., 2006. Erosion rates at the Mars exploration rover landing sites and long-term climate change on Mars. J. Geophys. Res. 111 (E12) https://doi.org/10.1029/2006JE002754.
Gordon, A.D., 1999. Classification. CRC Press.
Gower, J.C., 1971. A general coefficient of similarity and some of its properties. Biometrics 857–871.
Hauber, E., Kronberg, P., 2005. The large Thaumasia graben on Mars: is it a rift? J. Geophys. Res. Planets 110, 1–13. https://doi.org/10.1029/2005JE002407.
Kaas, O., Šilhavý, J., Kolingerová, I., Čada, V., 2023. Accelerated multi-hillshade hierarchic clustering for automatic lineament extraction. J. Geogr. Syst. 1–18. https://doi.org/10.1007/s10109-023-00423-y.
Karagoz, O., Kenkmann, T., Hergarten, S., 2024. Unraveling the tectonic history of the Tharsis rise on Mars: plume migration and critical taper dome. J. Geophys. Res. 129 https://doi.org/10.1029/2023JE007965 e2023JE007965.
Kaufman, L., Rousseeuw, P.J., 1990. Finding Groups in Data: an Introduction to Cluster Analysis. John Wiley & Sons. https://doi.org/10.1002/9780470316801.
Lachenbruch, A.H., 1961. Depth and spacing of tension cracks. J. Geophys. Res. 66 (12), 4273–4292.
Lucchetti, A., Rossi, C., Mazzarini, F., Pajola, M., Pozzobon, R., Massironi, M., Cremonese, G., 2021. Equatorial grooves distribution on Ganymede: length and self-similar clustering analysis. Planet. Space Sci. 195, 105140 https://doi.org/10.1016/j.pss.2020.105140.
Lucianetti, G., Cianfarra, P., Mazza, R., 2017. Lineament domain analysis to infer groundwater flow paths: clues from the pale di san Martino fractured aquifer, eastern Italian Alps. Geosphere 13, 1729–1746. https://doi.org/10.1130/GES01500.1.
Man, B., Rothery, D.A., Balme, M.R., Conway, S.J., Wright, J., 2023. Widespread small grabens consistent with recent tectonism on mercury. Nat. Geosci. 16 (10), 856–862. https://doi.org/10.1038/s41561-023-01281-5.
Mazzarini, F., 2004. Volcanic vent self-similar clustering and crustal thickness in the northern Main Ethiopian rift. Geophys. Res. Lett. 31 (4) https://doi.org/10.1029/2003GL018574.
Mazzarini, F., 2007. Vent distribution and crustal thickness in stretched continental crust: the case of the Afar depression (Ethiopia). Geosphere 3 (3), 152–162. https://doi.org/10.1130/GES00070.1.
Mazzarini, F., D'Orazio, M., 2003. Spatial distribution of cones and satellite-detected lineaments in the Pali Aike volcanic field (southernmost Patagonia): insights into the tectonic setting of a Neogene rift system. J. Volcanol. Geotherm. Res. 125 (3–4), 291–305. https://doi.org/10.1016/S0377-0273(03)00120-3.
Mazzarini, F., Isola, I., 2010. Monogenetic vent self-similar clustering in extending continental crust: examples from the east African rift system. Geosphere 6 (5), 567–582. https://doi.org/10.1130/GES00569.1.
Mazzarini, F., Isola, I., 2021. Vent distribution and structural inheritance in an embryonic rift: the example of the Chyulu Hills off-rift magmatic range (South Kenya). J. Volcanol. Geotherm. Res. 416, 107268 https://doi.org/10.1016/j.jvolgeores.2021.107268.
Mazzarini, F., Isola, I., 2022. Quaternary off-rift volcanism along a section of the east African rift system (EARS), from the South Ethiopia to the South Kenya. Ital. J. Geosci. 141 (3), 334–347. https://doi.org/10.3301/IJG.2022.19.
Mirkin, B., 2013. Mathematical Classification and Clustering, vol. 11. Springer Science & Business Media.
Mojena, R., 1977. Hierarchical grouping methods and stopping rules: an evaluation. Comput. J. 20 (4), 359–363. https://doi.org/10.1093/comjnl/20.4.359.
Montgomery, D.R., Som, S.M., Jackson, M.P.A., Schreiber, B.C., Gillespie, A.R., Adams, J. B., 2009. Continental-scale salt tectonics on Mars and the origin of Valles Marineris and associated outflow channels. Bull. Geol. Soc. Am. 121, 117–133. https://doi.org/10.1130/B26307.1.
Müllner, D., 2013. Fastcluster: fast hierarchical, agglomerative clustering routines for R and Python. J. Stat. Softw. 53, 1–18. https://doi.org/10.18637/jss.v053.i09.
Murtagh, F., Legendre, P., 2014. Ward's hierarchical agglomerative clustering method: which algorithms implement Ward's criterion? J. Classif. 31, 274–295. https://doi.org/10.1007/s00357-014-9161-z.
Ouillon, G., Castaing, C., Sornette, D., 1996. Hierarchical geometry of faulting. J. Geophys. Res. Solid Earth 101 (B3), 5477–5487. https://doi.org/10.1029/95JB02242.
Paasche, H., Eberle, D.G., 2009. Rapid integration of large airborne geophysical data suites using a fuzzy partitioning cluster algorithm: a tool for geological mapping and mineral exploration targeting. Explor. Geophys. 40 (3), 277–287. https://doi.org/10.1071/EG08028.
Perrin, C., Jacob, A., Lucas, A., Myhill, R., Hauber, E., Batov, A., Fuji, N., 2022. Geometry and segmentation of Cerberus Fossae, Mars: implications for marsquake properties. J. Geophys. Res. 127 (1) https://doi.org/10.1029/2021JE007118 e2021JE007118.
Pieterek, B., Brož, P., Hauber, E., Stephan, K., 2024. Insight from the Noachian-aged fractured crust to the volcanic evolution of Mars: a case study from the Thaumasia graben and Claritas fossae. Icarus 407, 115770. https://doi.org/10.1016/j.icarus.2023.115770.
Plescia, J.B., 2003. Cerberus Fossae, Elysium, Mars: a source for lava and water. Icarus 164 (1), 79–95. https://doi.org/10.1016/S0019-1035(03)00139-8.

Plescia, J.B., Saunders, R.S., 1982. Tectonic history of the Tharsis region, Mars. J. Geophys. Res. 87, 9775. https://doi.org/10.1029/JB087iB12p09775.
Pozzobon, R., Mazzarini, F., Massironi, M., Marinangeli, L., 2015. Self-similar clustering distribution of structural features on Ascraeus Mons (Mars): implications for magma chamber depth. Geological Society, London, Special Publications 401 (1), 203–218.
Prabhakaran, R., Bertotti, G., Urai, J., Smeulders, D., 2021. Investigating spatial heterogeneity within fracture networks using hierarchical clustering and graph distance metrics. Solid Earth 12 (10), 2159–2209. https://doi.org/10.5194/se-12-2159-2021.
Riedel, W., 1929. Zur Mechanik geologischer Brucherscheinungen ein Beitrag zum Problem der Fiederspatten. Zentbl. Miner. Geol. Palaont. Abt. 354–368.
Rossi, C., Cianfarra, P., Salvini, F., Mitri, G., Massé, M., 2018. Evidence of transpressional tectonics on the Uruk sulcus region, Ganymede. Tectonophysics 749, 72–87. https://doi.org/10.1016/j.tecto.2018.10.026.
Rossi, C., Cianfarra, P., Salvini, F., Bourgeois, O., Tobie, G., 2020. Tectonics of Enceladus' south pole: block rotation of the Tiger stripes. J. Geophys. Res. 125 (12) https://doi.org/10.1029/2020JE006471 e2020JE006471.
Rousseeuw, P.J., 1987. Silhouettes: a graphical aid to the interpretation and validation of cluster analysis. J. Comput. Appl. Math. 20, 53–65.
Schwenker, F., Trentin, E., 2014. Pattern classification and clustering: a review of partially supervised learning approaches. Pattern Recogn. Lett. 37, 4–14. https://doi.org/10.1016/j.patrec.2013.10.017.
Šilhavý, J., Minár, J., Mentlík, P., Sládek, J., 2016. A new artefacts resistant method for automatic lineament extraction using multi-Hillshade hierarchic clustering (MHHC). Comput. Geosci. 92, 9–20. https://doi.org/10.1016/j.cageo.2016.03.015.
Smith, M.R., Gillespie, A.R., Montgomery, D.R., Batbaatar, J., 2009. Crater-fault interactions: a metric for dating fault zones on planetary surfaces. Earth Planet. Sci. Lett. 284, 151–156. https://doi.org/10.1016/j.epsl.2009.04.025.
Sneath, P.H., Sokal, R.R., 1973. Numerical Taxonomy. The Principles and Practice of Numerical Classification.
Storti, F., Rossetti, F., Läufer, A.L., Salvini, F., 2006. Consistent kinematic architecture in the damage zones of intraplate strike-slip fault systems in North Victoria land, Antarctica and implications for fault zone evolution. J. Struct. Geol. 28, 50–63. https://doi.org/10.1016/j.jsg.2005.09.004.
Struyf, A., Hubert, M., Rousseeuw, P., 1997. Clustering in an object-oriented environment. J. Stat. Softw. 1, 1–30. https://doi.org/10.18637/jss.v001.i04.
Swanson, M.T., 1988. Pseudotachylyte-bearing strike-slip duplex structures in the fort foster brittle zone, S. Maine. J. Struct. Geol. https://doi.org/10.1016/0191-8141(88)90097-1.
Takahashi, A., Hashimoto, M., Hu, J.C., Takeuchi, K., Tsai, M.C., Fukahata, Y., 2019. Hierarchical cluster analysis of dense GPS data and examination of the nature of the clusters associated with regional tectonics in Taiwan. J. Geophys. Res. Solid Earth 124 (5), 5174–5191. https://doi.org/10.1029/2018JB016995.
Tanaka, K.L., Davis, P.A., 1988. Tectonic history of the Syria Planum province of Mars. J. Geophys. Res. Solid Earth 93, 14893–14917. https://doi.org/10.1029/JB093iB12p14893.
Tanaka, K.L., Golombek, M.P., Banerdt, W.B., 1991. Reconciliation of stress and structural histories of the Tharsis region of Mars. J. Geophys. Res. Planets 96, 15617–15633. https://doi.org/10.1029/91JE01194.
Tanaka, K.L., Skinner, J.A., Dohm, J.M., Irwin, R.P., Kolb, E.J., Fortezzo, C.M., Platz, T., Michael, G.G., Hare, T.M., 2014. Geologic Map of Mars: U.S. Geological Survey Scientific Investigations Map 3292, scale 1:20,000,000, pamphlet, 43 p. https://doi.org/10.3133/sim3292.
Tavani, S., Storti, F., Fernández, O., Muñoz, J.A., Salvini, F., 2006. 3-D deformation pattern analysis and evolution of the Añisclo anticline, southern Pyrenees. J. Struct. Geol. 28 (4), 695–712. https://doi.org/10.1016/j.jsg.2006.01.009.
Vaz, D.A., Spagnuolo, M.G., Silvestro, S., 2014. Morphometric and geometric characterization of normal faults on Mars. Earth Planet. Sci. Lett. 401, 83–94. https://doi.org/10.1016/j.epsl.2014.05.022.
Ward Jr., J.H., 1963. Hierarchical grouping to optimize an objective function. J. Am. Stat. Assoc. 58 (301), 236–244. https://doi.org/10.1080/01621459.1963.10500845.
Wise, D.U., Golombek, M.P., McGill, G.E., 1979. Tharsis province of Mars: geologic sequence, geometry, and a deformation mechanism. Icarus 38 (3), 456–472. https://doi.org/10.1016/0019-1035(79)90200-8.
Wise, D.U., Funiciello, R., Parotto, M., Salvini, F., 1985. Topographic lineament swarms: clues to their origin from domain analysis of Italy. Geol. Soc. Am. Bull. 96, 952. https://doi.org/10.1130/0016-7606(1985)96<952:TLSCTT>2.0.CO;2.
Yang, J., Grunsky, E., Cheng, Q., 2019. A novel hierarchical clustering analysis method based on Kullback–Leibler divergence and application on dalaimiao geochemical exploration data. Comput. Geosci. 123, 10–19. https://doi.org/10.1016/j.cageo.2018.11.003.
Yin, A., 2012. An episodic slab-rollback model for the origin of the Tharsis rise on Mars: implications for initiation of local plate subduction and final unification of a kinematically linked global plate-tectonic network on earth. Lithosphere 4, 553–593. https://doi.org/10.1130/L195.1.